Table III. Site-specific glycosylation analysis of the chymotryptic digest of apoB100 using LC/ESI MS/MS

Glycosylation site ID	Retention time (min)	Peptide theoretical MW[a]	Glycopeptides			Oligosaccharide			Composition[c]	Deduced Type[c]
			m/z	Charge	Calculated MW[a]	Calculated MW[a]	Theoretical MW[a]	Relative peak intensity (%)[b]		
G1	—	560.3	—	—	—	—	—	—	—	—
G2	11	822.3	1344.5	+2	2687.0	1882.7	1882.6	4	[HexNAc]2[Hex]9	High mannose
	11	822.3	1263.5	+2	2525.0	1720.7	1720.6	7	[HexNAc]2[Hex]8	High mannose
	11	822.3	1182.5	+2	2363.0	1558.7	1558.5	15	[HexNAc]2[Hex]7	High mannose
	12	822.3	1101.4	+2	2200.8	1396.5	1396.5	12	[HexNAc]2[Hex]6	High mannose
	12	822.3	1020.4	+2	2038.8	1234.5	1234.4	100	[HexNAc]2[Hex]5	High mannose
G3	12	1088.4	1001.8	+3	3002.4	1932.0	1931.7	70	[HexNAc]4[Hex]5[Neu5Ac]1	Biantennary complex
	15	1088.4	1098.8	+3	3293.4	2223.0	2222.8	100	[HexNAc]4[Hex]5[Neu5Ac]2	Biantennary complex
G4	14	318.1	768.4	+2	1534.8	1234.7	1234.4	—	[HexNAc]2[Hex]5	High mannose
G5	9	1021.4	963.1	+3	2886.3	1882.9	1882.6	100	[HexNAc]2[Hex]9	High mannose
	9	1021.4	1444.1	+2	2886.2	1882.8				
	9	1021.4	1363.1	+2	2724.2	1720.8	1720.6	40	[HexNAc]2[Hex]8	High mannose
	9[d]	1021.4	1282.1	+2	2562.2	1558.8	1558.5	16	[HexNAc]2[Hex]7	High mannose
G6	—	469.2	—	—	—	—	—	—	—	-
G7	—	1023.5	—	—	—	—	—	—	—	-
G8	—	515.3	—	—	—	—	—	—	—	-
G9	—	2846.4	—	—	—	—	—	—	—	-
G10	15	279.1	829.0	+3	2484.1	2223.0	2222.8	—	[HexNAc]4[Hex]5[Neu5Ac]2	Biantennary complex
	15	279.1	1243.0	+2	2484.0	2222.9				
G11	13	521.2	812.7	+3	2435.1	1931.9	1931.7	100	[HexNAc]4[Hex]5[Neu5Ac]1	Biantennary complex
	13	521.2	1218.5	+2	2435.0	1931.8				
	16	521.2	909.8	+3	2726.3	2223.0	2222.8	52	[HexNAc]4[Hex]5[Neu5Ac]2	Biantennary complex
G12	28	878.5	1028.8	+3	3083.4	2222.9	2222.8	—	[HexNAc]4[Hex]5[Neu5Ac]2	Biantennary complex
G13	44	978.5	1341.6	+2	2681.2	1720.7	1720.6	31	[HexNAc]2[Hex]8	High mannose
	44	978.5	1260.6	+2	2519.1	1558.6	1558.5	50	[HexNAc]2[Hex]7	High mannose
	44	978.5	1179.5	+2	2357.1	1396.6	1396.5	100	[HexNAc]2[Hex]6	High mannose

Table III. continued

Glycosylation site ID	Retention time (min)	Peptide theoretical MW[a]	Glycopeptides			Oligosaccharide			Composition[c]	Deduced Type[c]
			m/z	Charge	Calculated MW[a]	Calculated MW[a]	Theoretical MW[a]	Relative peak intensity (%)[b]		
	44	978.5	1098.5	2	2195.0	1234.5	1234.4	75	[HexNAc]2[Hex]5	High mannose
	35[d]	995.5*	1349.6	+2	2697.1	1719.6	1720.6	16	[HexNAc]2[Hex]8	High mannose
	35[d]	995.5*	1268.5	+2	2535.0	1557.5	1558.5	49	[HexNAc]2[Hex]7	High mannose
	35	995.5*	1187.5	+2	2373.0	1395.5	1396.5	100	[HexNAc]2[Hex]6	High mannose
	35	995.5*	1106.5	+2	2211.0	1233.5	1234.4	89	[HexNAc]2[Hex]5	High mannose
G14	35	995.5	954.4	+3	2860.3	1882.8	1882.6	—	[HexNAc]2[Hex]9	High mannose
	35	995.5	1431.2	+2	2860.3	1882.8				
G15	24	1128.5	1173.5	+2	2345.0	1234.6	1234.4	3	[HexNAc]2[Hex]5	High mannose
	24[d]	1128.5	1275.0	+2	2548.0	1437.5	1437.5	9	[HexNAc]3[Hex]5	Hybrid
	27	1128.5	1015.1	+3	3042.4	1931.9	1931.7	100	[HexNAc]4[Hex]5[Neu5Ac]1	Biantennary complex
	27	1128.5	947.4	+3	2839.3	1728.8	1728.6	79	[HexNAc]3[Hex]5[Neu5Ac]1	Hybrid
	27	1128.5	893.4	+3	2677.3	1566.8	1566.6	23	[HexNAc]3[Hex]4[Neu5Ac]1	Monoantennary complex
	30	1128.5	1112.2	+3	3333.5	2223.0	2222.8	28	[HexNAc]4[Hex]5[Neu5Ac]2	Biantennary complex
G16	—	550.2	—	—	—	—	—	—	—	-
G17	28	490.2	899.4	+3	2695.2	2223.0	2222.8	—	[HexNAc]4[Hex]5[Neu5Ac]2	Biantennary complex
	28	490.2	1348.5	+2	2695.0	2222.8				
G18	21	1082.6	999.8	+3	2996.4	1931.8	1931.7	100	[HexNAc]4[Hex]5[Neu5Ac]1	Biantennary complex
	25	1082.6	1096.8	+3	3287.4	2222.8	2222.8	51	[HexNAc]4[Hex]5[Neu5Ac]2	Biantennary complex
	37	1229.6[†]	786.9	+4	3143.5	1931.9	1931.7	100	[HexNAc]4[Hex]5[Neu5Ac]1	Biantennary complex
	37	1229.6[†]	1048.8	+3	3143.5	1931.8				
	38	1229.6[†]	994.8	+3	2981.5	1769.9	1769.6	14	[HexNAc]4[Hex]4[Neu5Ac]1	Biantennary complex
	40	1229.6[†]	859.7	+4	3434.6	2223.0	2222.8	67	[HexNAc]4[Hex]5[Neu5Ac]2	Biantennary complex
	40	1229.6[†]	1145.9	+3	3434.6	2223.0				
G19	37	736.4	884.4	+3	2650.3	1931.9	1931.7	100	[HexNAc]4[Hex]5[Neu5Ac]1	Biantennary complex
	37	736.4	1326.1	+2	2650.2	1931.8				
	40	736.4	981.4	+3	2941.2	2222.8	2222.8	94	[HexNAc]4[Hex]5[Neu5Ac]2	Biantennary complex

[a]Monoisotopic mass value.
[b]Relative peak intensity was calculated by comparing same chage state glycopeptide ions. The intensity of glycoform with maximum intensity at each glycosylation site was considered as 100%.
[c]The oligosaccharide composition and type were deduced from its composition.
[d]Product ion spectra were not acquired. These ions were considered as glycopeptides by the mass differences of 162(Hex) or 203(HexNAc) from the glycopeptides.
*The glycopeptides including G13 were found to be oxidized at methionine residue.
[†]Peptides of these glycopeptides including G18 were found as missed cleaved. The peptide sequence was considered as SKVHN[4210]GSEILF.

Table IV. Summary of apoB100 oligosaccharide structure obtained from tryptic digest and chymotryptic digest

Glycosylation site ID	Deduced oligosaccharide composition[a]					Deduced oligosaccharide type[a]
G1	Not glycosylated					—
G2	[HexNAc]2[Hex]9	[HexNAc]2[Hex]8	[HexNAc]2[Hex]7	[HexNAc]2[Hex]6	[HexNAc]2[Hex]5	High mannose
G3	[HexNAc]4[Hex]5[Neu5Ac]1	[HexNAc]4[Hex]5[Neu5Ac]2				Biantennary complex
G4	[HexNAc]2[Hex]5					High mannose
G5	[HexNAc]2[Hex]9	[HexNAc]2[Hex]8	[HexNAc]2[Hex]7			High mannose
G6	[HexNAc]2[Hex]5					High mannose
	[HexNAc]3[Hex]7[Neu5Ac]1	[HexNAc]3[Hex]6[Neu5Ac]1	[HexNAc]3[Hex]5[Neu5Ac]1			Hybrid
	[HexNAc]3[Hex]4[Neu5Ac]1					Monoantennary complex
	[HexNAc]4[Hex]4[Neu5Ac]1	[HexNAc]4[Hex]5[Neu5Ac]1	[HexNAc]4[Hex]5[Neu5Ac]2			Biantennary complex
G7	[HexNAc]4[Hex]5[Neu5Ac]1	[HexNAc]4[Hex]5[Neu5Ac]2				Biantennary complex
G8	Not glycosylated					—
G9	[HexNAc]4[Hex]5[Neu5Ac]2					Biantennary complex
G10	[HexNAc]4[Hex]5[Neu5Ac]1	[HexNAc]4[Hex]5[Neu5Ac]2				Biantennary complex
G11	[HexNAc]4[Hex]5[Neu5Ac]1	[HexNAc]4[Hex]5[Neu5Ac]2				Biantennary complex
G12	[HexNAc]4[Hex]5[Neu5Ac]2					Biantennary complex
G13	[HexNAc]2[Hex]8	[HexNAc]2[Hex]7	[HexNAc]2[Hex]6	[HexNAc]2[Hex]5		High mannose
G14	[HexNAc]2[Hex]9					High mannose
G15	[HexNAc]2[Hex]5					High mannose
	[HexNAc]3[Hex]6	[HexNAc]3[Hex]5	[HexNAc]3[Hex]6[Neu5Ac]1	[HexNAc]3[Hex]5[Neu5Ac]1		Hybrid
	[HexNAc]3[Hex]4[Neu5Ac]1					Monoantennary complex
	[HexNAc]4[Hex]4	[HexNAc]4[Hex]5	[HexNAc]4[Hex]4[Neu5Ac]1	[HexNAc]4[Hex]5[Neu5Ac]1	[HexNAc]4[Hex]5[Neu5Ac]2	Biantennary complex
	[HexNAc]4[Hex]5[Neu5Ac]1[Fuc]1					Biantennary complex
G16	[HexNAc]3[Hex]4[Neu5Ac]1					Monoantennary complex
	[HexNAc]4[Hex]4[Neu5Ac]1	[HexNAc]4[Hex]5[Neu5Ac]1	[HexNAc]4[Hex]5[Neu5Ac]2			Biantennary complex
G17	[HexNAc]4[Hex]5[Neu5Ac]1	[HexNAc]4[Hex]5[Neu5Ac]2				Biantennary complex
	[HexNAc]5[Hex]6[Neu5Ac]2					Triantennary complex
G18	[HexNAc]4[Hex]4[Neu5Ac]1	[HexNAc]4[Hex]5[Neu5Ac]1	[HexNAc]4[Hex]5[Neu5Ac]2			Biantennary complex
G19	[HexNAc]4[Hex]5[Neu5Ac]1	[HexNAc]4[Hex]5[Neu5Ac]2				Biantennary complex

[a]The oligosaccharide structure was deduced from the molecular weight and previously reported oligosaccharide structures of apoB100.

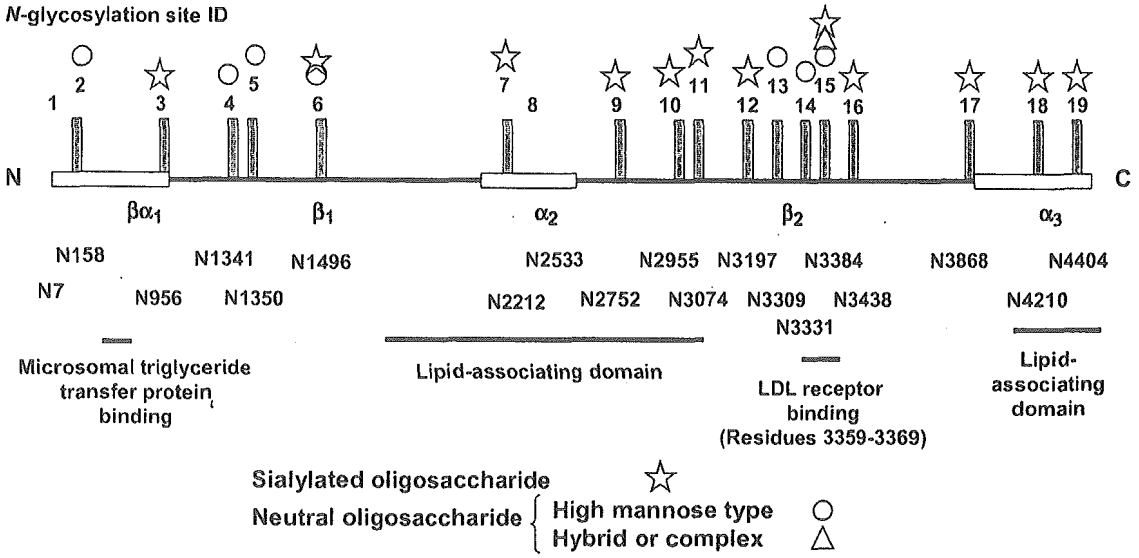

Fig. 7. *N*-glycosylation site of apoB100 and *N*-glycans at each site. *N*-glycosylation sites were shown on the pentapartite structure model, NH_3-$\beta\alpha_1$-β_1-α_2-β_2-α_3-COOH, previously reported (Segrest *et al.*, 1994). Circle, triangle, and star indicate high-mannose type oligosaccharides, neutral hybrid or neutral complex oligosaccharides, and mono- or disialylated oligosaccharides, respectively. High-mannose type oligosaccharides were found around the *N*-terminal and near the LDL–receptor binding site, and the other sites were attached by mono- or disialylated oligosaccharides. These oligosaccharide structures may reflect the local 3D structure of VLDL/LDL and may play a biological role.

the peptide containing the *N*-linked glycosylation site, we could directly deduce the peptide moiety. The molecular weight of the oligosaccharide moiety was calculated from the observed molecular weight of the glycopeptide and the theoretical molecular weight of the identified peptide. The carbohydrate composition and structure were deduced from the calculated molecular weight of the oligosaccharide. (2) There were relatively intense peaks of the peptide and peptide + GlcNAc ions in the glycopeptide product ion spectrum. Thus the *m/z* difference of 203 between fragment ions in the product ion spectrum could suggest the molecular weight of the peptide moiety. The peptide was determined from this suggested molecular weight and the molecular weight of the peptides containing the putative *N*-glycosylation site. The molecular weight of the carbohydrate was calculated, and the carbohydrate composition and structure were deduced. (3) Possible glycopeptide masses were calculated from the peptide masses containing the *N*-linked glycosylation site and possible *N*-linked oligosaccharide masses. The possible glycopeptide mass with the measured mass of the glycopeptide was identified. Assignment of peptide moiety was confirmed by the presence of the fragment ions derived from the peptide in the product ion spectrum.

The elution time as well as mass of a glycopeptide is also helpful to elucidate the oligosaccharide structure. The glycopeptides were eluted following reversed-phase high-performance LC based on the peptide and further separated based on the structure of the attached oligosaccharide (Kawasaki *et al.*, 2004). The glycopeptides having the same amino acid sequence were eluted in order of the number of Neu5Ac. Our results show that LC/ESI MS/MS with high sensitivity and high detection resolution is a powerful technique for the site-specific glycosylation analysis of glycoprotein.

Our study revealed that 17 of the 19 potential *N*-glycosylation sites in apoB100 were glycosylated, and the diversity of oligosaccharides at each of these *N*-glycosylation sites was determined. The deduced oligosaccharide structures in the present study were consistent with the structures previously identified in apoB100 (Garner *et al.*, 2001). Asn2212, which was reported to be unglycosylated (Yang *et al.*, 1989), could be glycosylated. The *N*-glycan structures and patterns are very different at each site. Asn158, 1341, 1350, 3309, and 3331 were occupied by high-mannose type oligosaccharides. The other sites except Asn1496 and 3384 (G6 and G15) were predominantly occupied by mono- or disialylated biantennary complex type oligosaccharides, and no neutral oligosaccharides were detected. These sialylated glycans may play an important biological role. Asn1496 and 3384 were occupied by high-mannose, hybrid, and complex type *N*-linked oligosaccharides. Hybrid-type oligosaccharides were found only at these two sites. The oligosaccharides at Asn 3384 are most heterogeneous, and at least 12 different oligosaccharide structures were present. Neutral complex type and neutral hybrid type oligosaccharides were detected only at this site. It is unlikely that this oligosaccharide heterogeneity is due to the fact that the apoB100 used in this study was extracted from the pooled serum of normolipidemic subjects, because no hybrid type oligosaccharides were detected except at Asn1496 and 3384 in this study, and it was reported that the diversity of the oligosaccharides of apoB100 was highly conserved among subjects (Garner *et al.*, 2001; Taniguchi *et al.*, 1989). It may be suggested that the diversity of the oligosaccharides at each glycosylation site was also conserved among subjects.

The relationship between sialylation and LDL–receptor binding has been examined. Desialylation of LDL increased the internalization of LDL by aortic smooth muscle cells

(Filipovic *et al.*, 1979), macrophage (Fujioka *et al.*, 2000) and aortic intimal cells (Orekhov *et al.*, 1989), but had no effect on degradation in hepatocytes (Attie *et al.*, 1979). These findings appear controversial. Asn3309, 3331, and 3384 are located near the LDL–receptor binding site in apoB100 (residues 3359–3369). Our data showed that these glycosylation sites were populated by high-mannose type (at Asn3309 and 3331) or a variety of oligosaccharides, including neutral or sialylated oligosaccharides (at Asn3384). These findings may indicate that sialic acid residues of apoB100 did not play a significant role in LDL–receptor binding and that desialylated LDL might be internalized by another mechanism. Shireman and Fisher (1979) reported that the removal of carbohydrate from LDL did not alter its binding to fibroblasts. Thus the carbohydrate moieties of LDL might not have a significant role in LDL–receptor binding.

The most interesting observation was that the most heterogeneous oligosaccharides were found at the *N*-glycosylation site (Asn3384) nearest to the LDL–receptor binding site. ApoB100 enwraps the VLDL and LDL particle. The C-terminal crosses over near the LDL–receptor binding site and inhibits binding of VLDL to the LDL receptor (Boren *et al.*, 1998). Conversion of VLDL to smaller LDL allows interaction with the LDL receptor. It is likely that the size of the VLDL/LDL particle could affect the 3D conformation around here. Thus the variety of oligosaccharide at Asn3384 may reflect the local 3D conformation of the VLDL particle and accessibility of trimming and glycosyl transferase enzymes.

The procedure described in this article provides an easy and efficient method for the identification of glycosylation sites and oligosaccharide heterogeneity of glycoproteins. Site-specific glycosylation analysis of apoB100 revealed that the diversity of oligosaccharide was distinct at each site. These data provide information to understand the role of oligosaccharides of apoB100 in LDL particles

Materials and methods

Materials

Acetonitrile, formic acid, chymotrypsin, and guanidine hydrochloride were from Wako Pure Chemicals (Osaka, Japan). Tosylphenylalanine chloromethane (TPCK)-treated trypsin was from Sigma (St. Louis, MO). Human apoB100 was purchased from MP Biomedicals (Irvine, CA). This product is derived from pooled human plasma, which is not particularly high-fat plasma. The water used was obtained from a Milli-Q water system (Millipore, Bedford, MA). All other reagents were of the highest quality available.

Reduction and S-carboxymethylation of apoB100

ApoB100 (500 μg) was dissolved in 810 μl of 0.5 M Tris–HCl buffer (pH 8.5) that contained 8 M guanidine hydrochloride and 5 mM ethylenediamine tetra-acetic acid. After the addition of 6 μl 2-mercaptoethanol, the mixture was incubated for 2 h at 40°C. Then, 17 mg of monoiodoacetic acid was added, and the resulting mixture was incubated for 2 h at 40°C in the dark. The reaction mixture was applied to a PD-10 column (Amersham Pharmacia Biotech, Uppsala, Sweden) to remove the reagents, and the eluate was lyophilized.

Enzyme digestion of apoB100

Reduced and carboxymethylated apoB100 was redissolved in 500 μl 0.1 M Tris–HCl buffer (pH 8.0). Half of the reduced and carboxymethylated apoB100 was incubated with 0.02 μg/μl of TPCK-treated trypsin (1:50 w/w) for 2 h at 37°C and the rest was incubated with 0.04 μg/μl of chymotrypsin (1:25 w/w) for 72 h at 37°C. The enzyme digestions were stopped by storing at –20°C before analysis.

High-performance LC of trypsin or chymotrypsin-digested apoB100

Tryptic digest (4 μg, about 8 pmol) and chymotryptic digest (2 μg, about 4 pmol) were analyzed by LC/ESI MS/MS. High-performance LC was performed on a Paradigm MS 4 equipped with a Magic C18 column (0.2 × 50 mm, Michrome BioResources, Auburn, CA). The eluents consisted of water containing 2% (v/v) acetonitrile and 0.1% (v/v) formic acid (pump A) and 90% acetonitrile and 0.1% formic acid (pump B). Trypsin- or chymotrypsin-digested samples of apoB100 were eluted with 5% B for 10 min, followed by a liner gradient from 5% to 70% of pump B in 130 min at a flow rate of 2 μl/min.

ESI Q-TOF MS/MS

MS analyses were performed using a QSTAR Pulsar i quadrupole TOF mass spectrometer (AB/MDS Sciex, Toronto, Canada) equipped with a nano-electrospray ion source. The mass spectrometer was operated in the positive ion mode. The nanospray voltage was set at 2500 V. Mass spectra for MS analysis were acquired over *m/z* 1000–2000 and 700–2000 for tryptic and chymotryptic digests, respectively, and for MS/MS analysis, over *m/z* 100–2000. After every regular MS acquision, MS/MS acquision was performed against multiple charged ions. The molecular ions were selected by data-dependent acquiring in the quadrupole analyzer and fragmented in the hexapole collision cell. The collision energy was varied between 40 and 80 eV depending on the size and charge of the molecular ion. All signals were monoisotopically resolved. Accumulation time of spectra is 1.0 and 2.0 s for MS and MS/MS, respectively.

Acknowledgments

We thank Dr. Nishimaki-Mogami for helpful suggestions. This study was supported by a grant-in-aid for Research on Health Sciences focusing on Drug Innovation from the Japan Health Sciences Foundation.

Abbreviations

apoB100, apolipoprotein B100; ESI, electrospray ionization; LC, liquid chromatography; LDL, low-density lipoprotein; MS, mass spectrometry; TIC, total ion chromatogram; TOF, time of flight; TPCK, Tosylphenylalanine chloromethane; VLDL, very low-density lipoprotein.

References

Attie, A.D., Weinstein, D.B., Freeze, H.H., Pittman, R.C., and Steinberg, D. (1979) Unaltered catabolism of desialylated low-density lipoprotein in the pig and in cultured rat hepatocytes. *Biochem. J.*, **180**, 647–654.

Boren, J., Lee, I., Zhu, W., Arnold, K., Taylor, S., and Innerarity, T.L. (1998) Identification of the low density lipoprotein receptor-binding site in apolipoprotein B100 and the modulation of its binding activity by the carboxyl terminus in familial defective apo-B100. *J. Clin. Invest.*, **101**, 1084–1093.

Carr, S.A., Huddleston, M.J., and Bean, M.F. (1993) Selective identification and differentiation of *N*- and *O*-linked oligosaccharides in glycoproteins by liquid chromatography-mass spectrometry. *Protein Sci.*, **2**, 183–196.

Chen, S.H., Yang, C.Y., Chen, P.F., Setzer, D., Tanimura, M., Li, W.H., Gotto, A.M. Jr, and Chan, L. (1986) The complete cDNA and amino acid sequence of human apolipoprotein B-100. *J. Biol. Chem.*, **261**, 12918–12921.

Duffin, K.L., Welply, J.K., Huang, E., and Henion, J.D. (1992) Characterization of *N*-linked oligosaccharides by electrospray and tandem mass spectrometry. *Anal. Chem.*, **64**, 1440–1448.

Filipovic, I., Schwarzmann, G., Mraz, W., Wiegandt, H., and Buddecke, E. (1979) Sialic-acid content of low-density lipoproteins controls their binding and uptake by cultured cells. *Eur. J. Biochem.*, **93**, 51–55.

Fujioka, Y., Taniguchi, T., Ishikawa, Y., and Yokoyama, M. (2000) Significance of acidic sugar chains of apolipoprotein B-100 in cellular metabolism of low-density lipoproteins. *J. Lab. Clin. Med.*, **136**, 355–362.

Garner, B., Harvey, D.J., Royle, L., Frischmann, M., Nigon, F., Chapman, M.J., and Rudd, P.M. (2001) Characterization of human apolipoprotein B100 oligosaccharides in LDL subfractions derived from normal and hyperlipidemic plasma: deficiency of alpha-*N*-acetylneuraminyllactosyl-ceramide in light and small dense LDL particles. *Glycobiology*, **11**, 791–802.

Kawasaki, N., Ohta, M., Itoh, S., and Hayakawa, T. (2004) Analyses of glycopeptides and glycoproteins by liquid chromatography-mass spectrometry and liquid chromatography-tandem mass spectrometry. *Methods Mol. Biol.*, **251**, 263–274.

Knott, T.J., Pease, R.J., Powell, L.M., Wallis, S.C., Rall, S.C. Jr, Innerarity, T.L., Blackhart, B., Taylor, W.H., Marcel, Y., Milne, R., and others. (1986) Complete protein sequence and identification of structural domains of human apolipoprotein B. *Nature*, **323**, 734–738.

Law, S.W., Grant, S.M., Higuchi, K., Hospattankar, A., Lackner, K., Lee, N., and Brewer, H.B. Jr. (1986) Human liver apolipoprotein B-100 cDNA: complete nucleic acid and derived amino acid sequence. *Proc. Natl Acad. Sci. USA*, **83**, 8142–8146.

Ling, V., Guzzetta, A.W., Canova-Davis, E., Stults, J.T., Hancock, W.S., Covey, T.R., and Shushan, B.I. (1991) Characterization of the tryptic map of recombinant DNA derived tissue plasminogen activator by high-performance liquid chromatography-electrospray ionization mass spectrometry. *Anal. Chem.*, **63**, 2909–2915.

Orekhov, A.N., Tertov, V.V., Mukhin, D.N., and Mikhailenko, I.A. (1989) Modification of low density lipoprotein by desialylation causes lipid accumulation in cultured cells: discovery of desialylated lipoprotein with altered cellular metabolism in the blood of atherosclerotic patients. *Biochem. Biophys. Res. Commun.*, **162**, 206–211.

Segrest, J.P., Jones, M.K., Mishra, V.K., Anantharamaiah, G.M., and Garber, D.W. (1994) ApoB-100 has a pentapartite structure composed of three amphipathic alpha-helical domains alternating with two amphipathic beta-strand domains. Detection by the computer program LOCATE. *Arterioscler Thromb.*, **14**, 1674–1685.

Shireman, R.B. and Fisher, W.R. (1979) The absence of a role for the carbohydrate moiety in the binding of apolipoprotein B to the low density lipoprotein receptor. *Biochim. Biophys. Acta*, **572**, 537–540.

Taniguchi, T., Ishikawa, Y., Tsunemitsu, M., and Fukuzaki, H. (1989) The structures of the asparagine-linked sugar chains of human apolipoprotein B-100. *Arch. Biochem. Biophys.*, **273**, 197–205.

Vukmirica, J., Nishimaki-Mogami, T., Tran, K., Shan, J., McLeod, R.S., Yuan, J., and Yao, Z. (2002) The N-linked oligosaccharides at the amino terminus of human apoB are important for the assembly and secretion of VLDL. *J. Lipid. Res.*, **43**, 1496–1507.

Yang, C.Y., Chen, S.H., Gianturco, S.H., Bradley, W.A., Sparrow, J.T., Tanimura, M., Li, W.H., Sparrow, D.A., DeLoof, H., Rosseneu, M., and others. (1986) Sequence, structure, receptor-binding domains and internal repeats of human apolipoprotein B-100. *Nature*, **323**, 738–742.

Yang, C.Y., Gu, Z.W., Weng, S.A., Kim, T.W., Chen, S.H., Pownall, H.J., Sharp, P.M., Liu, S.W., Li, H.W., Gotto, A.M. Jr., and Chan, L. (1989) Structure of apolipoprotein B-100 of human low density lipoproteins. *Arteriosclerosis*, **9**, 96–108.

J Pharmacol Sci 97, 361 – 368 (2005)

Journal of Pharmacological Sciences

Full Paper

Simultaneous Real-Time Detection of Initiator- and Effector-Caspase Activation by Double Fluorescence Resonance Energy Transfer Analysis

Hiroshi Kawai[1], Takuo Suzuki[1], Tetsu Kobayashi[1], Haruna Sakurai[2], Hisayuki Ohata[2], Kazuo Honda[2], Kazutaka Momose[2], Iyuki Namekata[3], Hikaru Tanaka[3], Koki Shigenobu[3], Ryu Nakamura[4], Takao Hayakawa[1], and Toru Kawanishi[1,*]

[1]*Division of Biological Chemistry and Biologicals, National Institute of Health Sciences, Tokyo 158-8501, Japan*
[2]*Department of Pharmacology, School of Pharmaceutical Sciences, Showa University, Tokyo 142-8555, Japan*
[3]*Department of Pharmacology, Toho University School of Pharmaceutical Sciences, Chiba 274-8510, Japan*
[4]*Carl Zeiss Co., Ltd., Tokyo 160-0003, Japan*

Received August 31, 2004; Accepted January 8, 2005

Abstract. Fluorescence resonance energy transfer (FRET) with green fluorescent protein (GFP) variants has become widely used for biochemical research. In order to expand the choice of fluorescent range in FRET analysis, we designed various color versions of the FRET-based probes for caspase activity, in which the substrate sequence of the caspase was sandwiched by donor and acceptor fluorescent proteins, and studied the potential of these color versions as fluorescent indicators. Six color versions were constructed by a combination of cyan fluorescent protein (CFP), GFP, yellow fluorescent protein (YFP), and DsRed. Real-time monitoring in single cells revealed that all probes could detect caspase activation during tumor necrosis factor (TNF)-α-induced cell death as a fluorescent change. GFP-DsRed and YFP-DsRed were as sensitive as CFP-YFP, and CFP-DsRed also showed a large fluorescent change. By using two probes, CFP-DsRed and YFP-DsRed, we carried out simultaneous multi-FRET analysis and revealed that the initiator- and effector-caspases were activated almost simultaneously in TNF-α-induced cell death. These findings may give experimental bases for the development of novel techniques to analyze multi-events simultaneously in single cells by using FRET probes in combination.

Keywords: fluorescence resonance energy transfer, green fluorescent protein, tumor necrosis factor-α, cell death, caspase

Introduction

Many probes for various physiological reactions have been developed with green fluorescent protein (GFP) variants by using a similar strategy as that used with cameleon, the Ca^{2+}-sensing fusion protein developed by Miyawaki et al. (1 – 9). The cameleon consists of cyan fluorescent protein (CFP), calmodulin, M13 peptide, and yellow fluorescent protein (YFP). This fusion protein senses Ca^{2+} as the change of fluorescence resonance energy transfer (FRET) efficiency between CFP and YFP. Calmodulin binds M13 in the presence of Ca^{2+}, which causes conformational change in cameleon, resulting in a change in the distance between and relative orientation of CFP and YFP. This change alters the FRET efficiency from CFP to YFP; therefore, Ca^{2+} can be monitored as the fluorescent change (1).

CFP and YFP are the most frequently used pair for analysis by FRET. This pair is suitable for FRET analysis because the spectral overlap between the emission of the donor protein (CFP) and the excitation of the acceptor protein (YFP) is sufficient for energy transfer, and their ranges of fluorescence are far apart enough to be separated by measuring devices such as fluorescent microscopy (10). However, there are limitations for the CFP-YFP pair. It is impossible, for example, to use the CFP-YFP FRET probe for simultaneous measurement with other probes that are made of GFP variants or have

*Corresponding author. FAX: +81-3-3700-9064
E-mail: kawanish@nihs.go.jp.

fluorescein structure. If more choice of FRET probes is available from wider fluorescence ranges, it would allow us to analyze multi-events simultaneously occurring in living cells.

In this paper, we developed caspase-sensors of various colors by using cyan, green, yellow, and red fluorescent proteins and assessed their ability to detect the caspase activation in living single cells. Based on the findings obtained, we tried to perform multi-event FRET analysis and clarify the temporal relationships between biochemical reactions during cell death.

Materials and Methods

Plasmid construction

Plasmid encoding CY-sensor, YFP-peptide-CFP, was generated as previously reported (11). The sequence encoding 11 amino acids at the C-terminus of YFP was eliminated in this construct. The C-terminal truncated forms of the CFP (or GFP) gene were generated by PCR with primers containing the NheI site or BspEI site and pECFP-C1 (or pEGFP-C1; Clontech, Palo Alto, CA, USA) as a template, and the restricted fragment was inserted into the NheI/BspEI sites of the CY-sensor to generate a plasmid carrying truncated CFP (or GFP) at the N-terminus. DsRed was generated from pDsRed2-C1 (Clontech) by PCR, at the AgeI/NotI sites, and the restricted fragment was inserted into the AgeI/NotI sites of the CY-sensor to generate a plasmid carrying DsRed2 at the C-terminus. CG-, CR-, GR-, and YR-sensors were generated with a combination of these elements. The AgeI/BsrGI fragment from pEGFP-C1 was inserted into the AgeI/BsrGI sites of the CY-sensor to generate the GY-sensor. All cloned sequences were verified by sequencing.

Cell culture and transfection

HeLa cells were cultured in DMEM (Sigma-Aldrich, St. Louis, MO, USA) supplemented with 100 units/ml of penicillin G, 100 μg/ml of streptomycin, and 10% fetal calf serum (Invitrogen Corp., Carlsbad, CA, USA). Plasmid encoding the sensor protein was transfected into HeLa cells using Effectene Transfection Reagent (Qiagen, Hilden, Germany) according to the manufacturer's instructions. After 12 – 24 h incubation with the transfection reagent, the cells were washed with PBS and cultivated on dishes suitable for assay in medium containing 500 μg/ml of G418 for an additional 1 – 3 days until the assay was performed.

Western blotting

Cells cultured in a plastic dish were washed with PBS and lysed with 1 × SDS loading buffer. The samples dissolved in 1 × SDS loading buffer were incubated at 95°C for 2 min, and then they were loaded onto SDS-polyacrylamide gels (10%). Proteins were separated at 20 mA and then blotted to PVDF membranes in Tris-glycine transfer buffer at 100 V for 2 h. The membrane was incubated with block ace (Dainippon Pharmaceutical, Osaka) for 1 h, anti-GFP peptide antibody (Clontech, diluted with 0.1 × block ace to 1:1,000) for 2 h, and anti-rabbit IgG horseradish peroxidase-conjugated secondary antibody (Chemicon International Inc., Temecula, CA, USA; diluted with 0.1 × block ace to 1:10,000) for 1 h. The membrane was washed with TBS-T 3 times for 5 min after the incubation with the antibody. All of these incubations were performed at room temperature. The membrane was developed with the ECL chemiluminescence detection reagent (Amersham Biosciences, Piscataway, NJ, USA).

Measurement of fluorescent spectra of the sensors in HeLa cells

Spectral imaging was performed with LSM510META (Carl Zeiss, Jena, Germany) (12). Cells expressing one of the sensors were observed by excitation light at 458 nm (Ar laser), emitted fluorescence was separated by a grating, and the separated fluorescence were detected by 24 photomultiplier tubes (PMT) that were set to detect fluorescence at 468 – 714 nm. Each PMT detected fluorescence in the 10.7-nm wavelength range. So, the fluorescent spectrum at 468 – 714 nm was obtained with 10.7-nm resolution. Cell death was induced by incubation with tumor necrosis factor (TNF)-α (100 ng/ml) and cycloheximide (CHX, 10 μg/ml) for 6 h. Fluorescent spectra of living and dead cells were obtained from the whole cell region of normal-shaped and spherical cells, respectively.

Real-time imaging with FRET sensors

Transfected cells were cultured on a cover glass (25-mm diameter, 0.15 – 0.18-mm thickness) for 1 – 3 days. Cells were treated with TNF-α/CHX and then incubated under the usual culture condition for 1 – 2 h before analysis. Analyses were carried out by confocal laser-scanning fluorescent microscopy using a Carl Zeiss LSM510 system. During the observation, the media were buffered with 10 mM hepes buffer (pH 7.4), and the cells were maintained at 35 – 37°C. DIC images and grayscale images for fluorescence channels were obtained every 2 min unless otherwise described. Excitation lights for the FRET probe (458 nm for the CG-, CY-, GY-, and CR-sensors; 488 nm for the GR- and YR-sensors) were provided by an Ar laser with a 458 or 488 dichroic mirror. Images of the FRET probe were obtained separately for both donor and acceptor

Table 1. Measurement conditions for real-time analysis by LSM510

Sensor	Fusion protein[a]	Excitation (nm)[b]	Emission (nm)[c]		
			beam splitter	emission filter	
				donor	acceptor
CG	GFP-peptide-CFP	458	515	467.5 – 497.5	515 – 545
CY	YFP-peptide-CFP	458	515	467.5 – 497.5	515 – 545
GY	YFP-peptide-GFP	458	515	475 – 525	515 – 545
CR	CFP-peptide-DsRed	458	515	467.5 – 497.5	560 – 615
GR	GFP-peptide-DsRed	488	545	505 – 530	560 – 615
YR	YFP-peptide-DsRed	488	545	505 – 530	560 – 615

[a]N-terminal CFP, GFP, and YFP were in a truncated form in which 11 amino acids at the C-terminus were eliminated, and His_{10} was present at the C-terminus of CG, CY, and GY. [b]Excitation light was obtained by Ar laser and a 458 or 488 dichroic mirror. [c]Emitted fluorescence was separated by a 515 or 545 dichroic mirror, and the fluorescence of the donor and that of the acceptor were obtained through band pass emission filters.

fluorescence using a dichroic mirror and band-pass emission filters as shown in Table 1. Images were processed and quantified using MetaFluor software as follows: The average pixel intensity of the fluorescence of the whole cell region was determined for each channel. The ratio value was calculated as the average pixel value of the fluorescent ratio, (fluorescent intensity for the acceptor channel) / (fluorescent intensity for the donor channel), in the whole cell region. As cells changed their morphology during the observation, the whole cell region was determined separately in each image.

Results

Construction and characterization of FRET probes

We developed plasmids expressing caspase sensors as shown in Fig. 1a. A 12-amino-acid peptide derived from poly(ADP-ribose)polymerase (PARP) that is a well-known substrate of effector caspases was sandwiched by two different fluorescent proteins (an example of CFP-YFP is shown in Fig. 1a). The peptide sequence contains a caspase recognition site in the middle, and this fusion protein was cleaved mainly by caspase-3 (11). CFP-GFP, CFP-YFP, GFP-YFP, CFP-DsRed, GFP-DsRed, and YFP-DsRed were used as the donor-acceptor pairs. We named these fusion proteins CG-, CY-, GY-, CR-, GR-, and YR-sensor, respectively (Table 1). These fusion proteins show FRET in their intact form, whereas in the presence of active caspase, the peptide sequence is cleaved, CFP and YFP are far apart, and the fusion proteins do not show FRET any longer. The fluorescent ratio of acceptor/donor reflects the amount of FRET, so we used the reduction of this value as an index of caspase activation.

HeLa cells expressing one of these fusion proteins

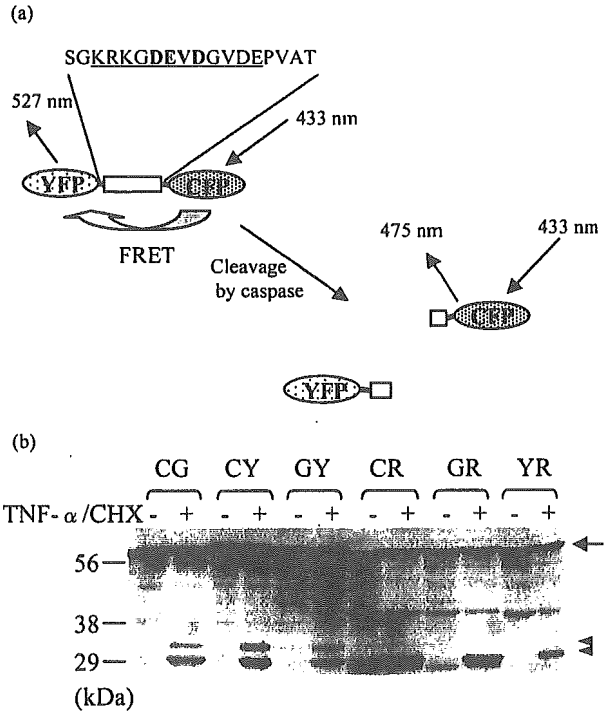

Fig. 1. Small peptide sandwiched by two different fluorescent proteins can be a caspase-sensor. a: Fusion protein that consists of a PARP-derived 12-amino-acid peptide sandwiched by CFP and YFP exhibits FRET in its intact form. In the presence of active caspases, the peptide is cleaved, and the fusion protein does not exhibit FRET. Caspase activation can be detected by measuring the fluorescence of CFP and YFP. b: Six caspase-sensors expressed in HeLa cells were cleaved by cell death stimuli. HeLa cells expressing one of the sensors were incubated in the presence or absence of TNF-α/CHX for 6 h. The arrow and arrowhead indicate the full length and cleaved fragments of the sensors.

were treated with TNF-α/CHX. After 6-h exposure, the sensor proteins in cells were extracted and analyzed by western blotting. All 6 fusion proteins were detected in their intact forms in non-treated HeLa cells (arrow in Fig. 1b), and small fragments were detected in cells treated with TNF-α/CHX (arrowhead in Fig. 1b), indicating that the fusion proteins were cleaved by cell death stimuli, as expected. The antibody used in this analysis reacts with CFP, GFP, and YFP, but not with DsRed. Therefore, CG-, CY-, and GY-sensor showed two cleaved fragments corresponding to the N- and C-terminal C/G/YFP, whereas CR-, GR-, and YR-sensor showed only one cleaved fragment corresponding to the N-terminal C/G/YFP.

Figure 2 shows the fluorescent spectra of the probes in living or dead cells. Comparing the fluorescence of living and dead cells, all sensors showed an increase of donor fluorescence and/or a reduction of acceptor fluorescence in response to cell death stimuli. This change results in a reduction of fluorescent ratio of acceptor/donor that is an index of FRET. These sensors were designed to show a reduction of FRET with caspase activation, so these results suggest that all 6 fusion proteins work as expected and can detect caspase activation as fluorescent change in living cells.

For simultaneous application of two or more fluorescent probes, minimum spectral overlap between probes is one of the important conditions. The spectra in Fig. 2 give us a clue to determine a suitable combination of probes for multi-probe analysis. CG-, CY-, or GY-sensor has the least fluorescence in the red-fluorescence region (>600 nm), so it is possible to use this fluorescent region for another dye. We can use a red-fluorescent dye that has fluorescence in this region together with CG-, CY-, or GY-sensor simultaneously. On the other hand, YR-sensor has the least fluorescence in the blue-cyan region (<500 nm), so blue-cyan-fluorescent dye is applicable with this probe for the purpose of simultaneous fluorescence imaging. The color variations of FRET probe may be useful for multi-probe analysis.

Real-time detection of caspase activation in living cells

Next, we applied the sensor proteins to real-time measurement. HeLa cells expressing one of the sensor proteins were analyzed with a time resolution of 2 min by laser-scanning confocal fluorescent microscopy. Figure 3 shows typical images (a) and fluorescent changes (b) during cell death. HeLa cells expressing GR-sensor were treated with TNF-α/CHX. An increase of donor protein fluorescence (GFP), a reduction of acceptor protein fluorescence (DsRed), and a reduction of the fluorescent ratio of acceptor/donor (DsRed/GFP) were observed in each cell at a different time. Caspases began to work at the point when the fluorescent ratio began to decrease.

All sensors showed similar changes, meaning that all sensors were useful for real-time detection of the caspase activation in a living cell, although the apparent sensitivity was different between sensors. In order to compare the sensitivity of these sensors to detect the caspase activation, the amount of the fluorescent change was calculated. We defined the start point and the end

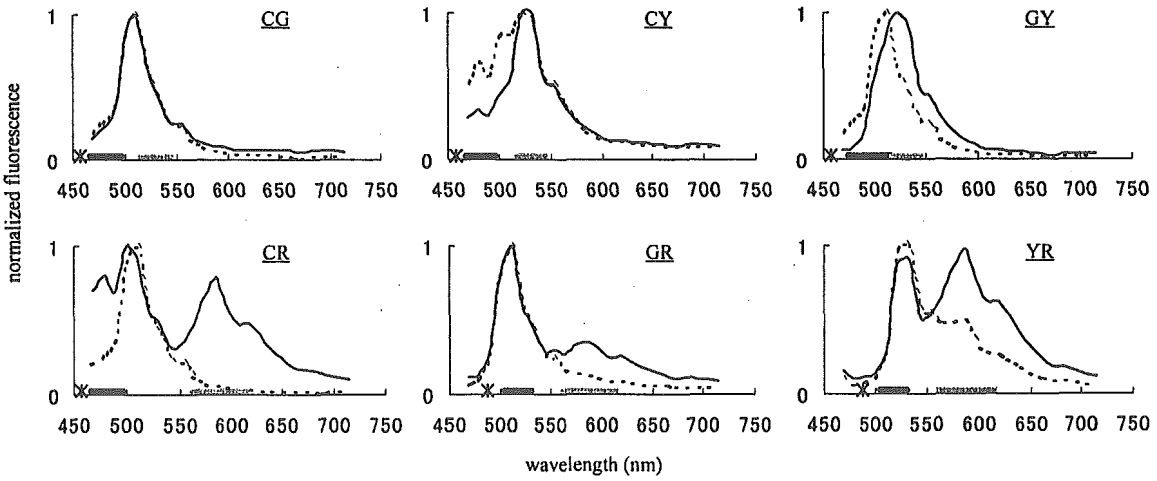

Fig. 2. Fluorescent spectra of the caspase-sensors in HeLa cells. HeLa cells expressing each sensor were treated with TNF-α/CHX for 6 h. The spectra of living cells (solid line) and dead cells (dotted line) were obtained from normal-shaped and spherical cells, respectively. Each spectrum was normalized to the peak that showed maximal intensity. The asterisks and bars on horizontal axes represent the excitation wavelength and detection range for the emitted fluorescence, respectively, used in real-time imaging analysis. Each spectrum is the average of data from 13 - 26 cells.

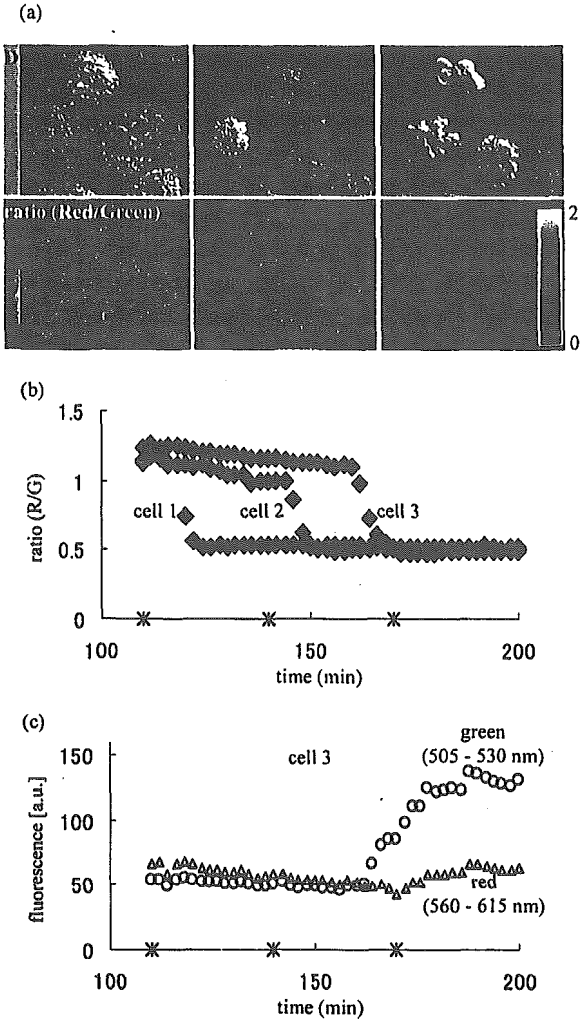

Fig. 3. Real-time imaging of caspase activation in living HeLa cells during cell death. HeLa cells expressing GR-sensor were treated with TNF-α/CHX, and fluorescent images were obtained every 2 min. a: DIC images (upper panels) and fluorescent ratios (Red/Green, lower panels) are shown in grayscale. The indicated time represents the time after the addition of TNF-α/CHX. Scale bar, 10 μm. b: The fluorescent ratio of cells were plotted. Cell 1, 2, or 3 corresponds to the cells shown in panel a. c: The mean pixel intensity in arbitrary fluorescent units (a.u.) for each channel was plotted. The fluorescence of cell No. 3 from panel a is shown. Open circle, GFP; open triangle, DsRed; closed diamond, ratio of Red/Green. Asterisks on the x-axis indicate the time points of the images in panel a.

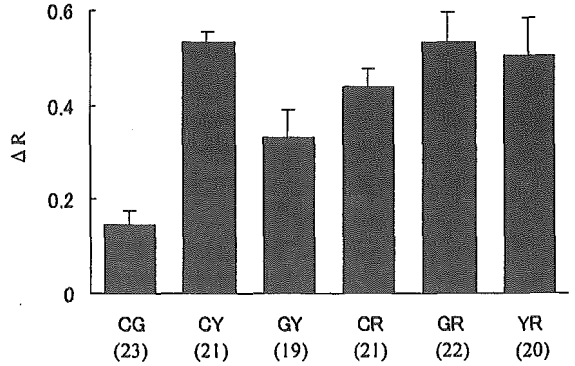

Fig. 4. Comparison of the sensitivity of various caspase-sensors. The amount of change of the fluorescent ratio during cell death (ΔR) was determined in each cell as described in the text. Bars represent means ± S.D. The number of cells used in each analysis is shown in parentheses.

point of the reduction of the fluorescent ratio as follows: the start point was the point after which the value decreased over four continuous points or more, the value decreased more than 10% in total, and the reduction of the value was not because of artificial noise such as focus shift; the end point followed the start point and was the point at which the value stopped decreasing. The sensitivity of the probe was calculated as $\Delta R = |(R_{end} - R_{start}) / R_{start}|$, where R_{start} and R_{end} were the fluorescent ratio at the start point and the end point, respectively. Figure 4 shows ΔR for each probe. GR and YR, as well as CY, showed the highest ΔR. They each showed a more than 50% change during cell death. CR showed a slightly lower ΔR, but its change was still 44% on average. CG and GY were less sensitive, probably because the fluorescent spectra of the donor and the acceptor were so similar that our system could not effectively measure FRET between them. CY *vs* GR, CY *vs* YR, or GR *vs* YR were not significantly different, and any other comparisons were significantly different by the Games-Howell test ($P<0.05$).

Simultaneous multi-event analysis using two FRET probes

Finally, we tried to perform multi-FRET measurement. We constructed a YR-initiator caspase sensor and a CR-effector caspase sensor by changing the caspase substrate sequence in the sensor and applied them to real-time imaging analysis simultaneously in order to reveal the temporal relationships between the initiator caspase activation and the effector caspase activation in the same cell. The caspase substrate sequences were derived from procaspase-3 and PARP, respectively, and their sequences are shown in Fig. 5a. These sensors were cleaved mainly by caspase-8/9 and caspase-3, respectively (11).

Simultaneous measurement of these sensors was performed under the multi-track scanning mode, in which two sets of excitation-detection conditions were used alternatively. CFP fluorescence by excitation at 458 nm was measured in the first track, and YFP and DsRed fluorescence by excitation at 488 nm was mea-

(a) YFP-SGLDCGIETDSGVDEPVAT-DsRed : YR-(IC)sensor
CFP-SGKRKGDEVDGVDEPVAT-DsRed : CR-(EC)sensor

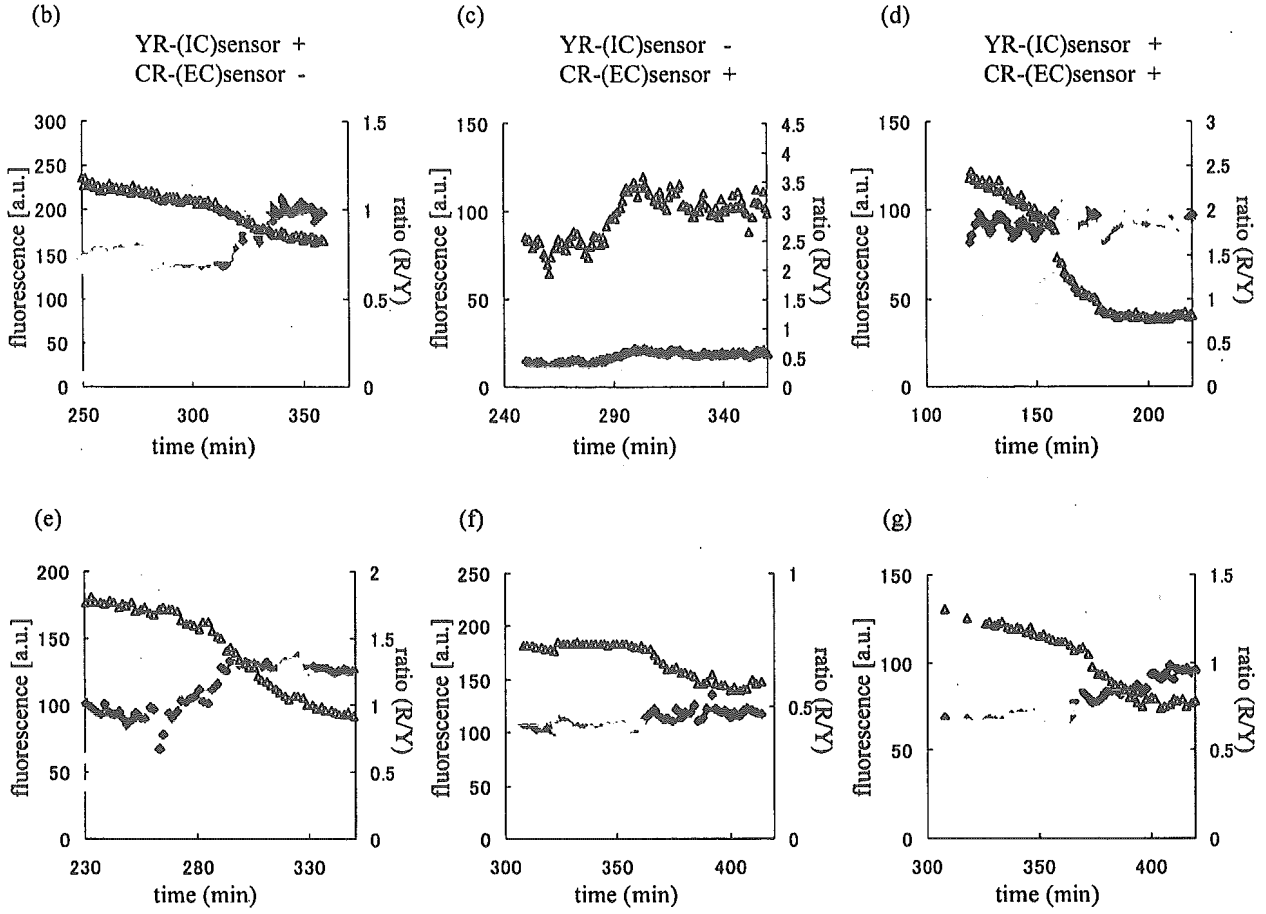

Fig. 5. Simultaneous measurement of initiator- and effector-caspase activation with YR-sensor and CR-sensor. HeLa cells expressing YR-initiator caspase sensor and/or CR-effector caspase sensor were treated with TNF-α/CHX and observed as described in the text. a: Probes used in this study. Underline indicates peptide derived from procaspase-3 and PARP, and bold indicates the consensus 4 amino acid sequence for caspase recognition. b – g: Cells expressing YR-initiator caspase sensor (b), CR-effector caspase sensor (c), or both of them (d – g) were treated with TNF-α/CHX. The fluorescence of CFP, YFP, and DsRed (colored plots) and the fluorescent ratio of DsRed/YFP (open triangles) were plotted against time after TNF-α/CHX treatment.

sured in the second track. The time difference of scanning between tracks is about 3 – 8 s. Figures 5b and 5c show control studies with cells expressing only one of the probes. These control studies were conducted in the same conditions as Fig. 5d. Figures 5b and 5c indicate that the YR- and CR-sensor could detect initiator- and effector-caspase activation as an increase of YFP and CFP signal, respectively, and the contamination of the signal between the YFP and CFP channels was negligible. So, we used an increase of the YFP and CFP signal as index of the initiator- and the effector-caspase activation, respectively. The DsRed signal in Fig. 5c was derived from direct excitation of DsRed in the CR-sensor by the excitation light at 488 nm and was increased when the cell shrank because fluorescent proteins were concentrated in the cell.

Figure 5d shows typical data of multi-probe analysis with the YR-initiator caspase sensor and CR-effector caspase sensor. In this cell, the fluorescence was dramatically changed at 150 – 160 min after TNF-α /CHX treatment. The YFP and CFP signal began to increase almost simultaneously, suggesting that initiator caspase and effector caspase were initially activated within a short time period. Figures 5e – 5g show three

other examples. We observed more than 30 cells in at least 3 independent experiments and found that all dying cells showed similar results.

Discussion

In this study, we developed various color versions of caspase-sensors with CFP, GFP, YFP, and DsRed and revealed that various combinations are applicable in FRET analysis. CY, CR, GR, and YR pairs are preferable FRET pairs that possess a high ability to detect the caspase activation.

The sensitivity shown in Fig. 4 represents the apparent FRET change that depends on the measuring system and was determined by three factors. 1) Intrinsic FRET efficiency: All 4 fluorescent proteins had different fluorescent characteristics; therefore, the levels of FRET efficiency in 6 probes differed from each other. 2) Excitation crosstalk: The acceptors were excited directly by the excitation light. 3) Emission crosstalk: The acceptor channel was contaminated with the donor signal, and vice versa, because the setting shown in Table 1 could not perfectly separate the signals from the donor and the acceptor. The differences in these factors cause the difference of sensitivity among the sensors. Factors 2) and 3) reduce the apparent FRET change in the measurement. In the case of the CG-sensor, for example, fluorescent spectrum of donor and acceptor are so similar that the intrinsic FRET efficiency may be high, but excitation and emission crosstalk may also be high, much higher than in other sensors (e.g., CY-sensor), resulting in the relatively low sensitivity of this probe in our measurement system. Crosstalk effects are undesirable for detection, but it is impossible to completely eliminate these effects in the current measurement system. Maybe we could obtain different results by using spectral imaging in which emission crosstalk is eliminated (12).

According to the characteristics of the fluorescence spectrum, the CY probe seems to be one of the best for FRET-detection. However, the probe is not suitable for imaging with confocal laser microscopy, because the normal argon ion laser, the most common one in confocal microscopes, is not suitable for the excitation of CFP. The blue laser is the most suitable for the excitation, but it is not common in confocal laser microscopes. In this paper, we had to use the argon ion laser emitting 458 nm and the special emission filters optimized for the confocal ratio-imagings of caspase activation using the CY probe (11). On the contrary, the GR probe and the YR probe can be efficiently excited at 488 nm emitted by the normal argon ion laser and imaged with a set of emission filters for fluorescein and a set for rhodamine, with which almost all of the confocal microscopes are equipped. In addition, the GR probe is useful for the detection of caspase activation in flow cytometry, because almost all of the normal flow cytometers are also usually equipped with the laser and the emission filters.

DsRed-containing "red"-sensors have several characteristics that are different from other "non red"-sensors. As previously reported (13), it takes longer for DsRed to mature and emit red fluorescence than it takes for GFPs, and DsRed fluorescence tends to decrease during real-time observation, which may cause a reduction of the apparent sensitivity. These characteristics must be considered when any analysis is performed with these sensors, but as shown in Figs. 4 and 5, red-sensors have a potential similar to that of the CY-sensor and are very useful for multi-color imaging.

It has been reported that DsRed is useful as a fusion tag and a partner for FRET (13, 14). Erickson et al. analyzed the potential of DsRed as a FRET partner with CFP and GFP (14). Mizuno et al. developed a Ca^{2+} sensing fusion protein using Sapphire and DsRed (13). And recently, Karasawa et al. used two novel fluorescent proteins, namely the cyan-emitted and orange-emitted fluorescent proteins from *Acropara* sp. and *Fungia concinna*, respectively, as a FRET pair, and measured caspase-3 activity in cells (15). These results combined with our results indicate that various fluorescent proteins including GFP derivatives, DsRed, and others are useful for FRET analysis. By choosing the appropriate two fluorescent proteins as the FRET pair, we can customize the fluorescent range of FRET-based imaging probes to fit the analysis, which would expand the flexibility of simultaneous multi-event analysis.

By using the CR and YR developed in this study, we were able to analyze two FRET probes simultaneously in the same cells. In several reports, the initiator caspase activity and the effector caspase activity were measured in living cells (8, 9, 11). In these reports, however, each activity was measured independently in different cells. To our knowledge, the present study is the first report that analyzes these activities in the same cell. The results directly reveal the temporal relationships between these caspase activities. It takes a long time for cells to start the initiator caspase activation after drug treatment, but it takes a relatively short time for cells to start the effector caspase activation after the initiator caspase activation. The caspase cascade is initiated at the last stage of cell death signaling, and it proceeds within a short time period.

Acknowledgments

This study was supported in part by a Grant-in-Aid for

Research on Health Sciences Focusing on Drug Innovation from the Japan Health Science Foundation; a Grant-in-Aid for Research on Advanced Medical Technology from the Ministry of Health, Labour, and Welfare; and a grant (MF-16) from the Organization for Pharmaceutical Safety and Research.

References

1 Miyawaki A, Llopis J, Heim R, Mccaffery JM, Adams JA, Ikura M, et al. Fluorescent indicators for Ca^{2+} based on green fluorescent proteins and calmodulin. Nature. 1997;388:882–887.

2 Zaccolo M, Giorgi FD, Cho CY, Feng L, Knapp T, Negulescu PA, et al. A genetically encoded, fluorescent indicator for cyclic AMP in living cells. Nat Cell Biol. 2000;2:25–29.

3 Nagai Y, Miyazaki M, Aoki R, Zama T, Inouye S, Hirose K, et al. A fluorescent indicator for visualizing cAMP-induced phosphorylation in vivo. Nat Biotechnol. 2000;18:313–316.

4 Kurokawa K, Mochizuki N, Ohba Y, Mizuno H, Miyawaki A, Matsuda M. A pair of fluorescent resonance energy transfer-based probes for tyrosine phosphorylation of the CrkII adaptor protein in vivo. J Biol Chem. 2001;276:31305–31310.

5 Sato M, Ozawa T, Inukai K, Asano T, Umezawa Y. Fluorescent indicators for imaging protein phosphorylation in single living cells. Nat Biotechnol. 2002;20:287–294.

6 Tyas L, Brophy VA, Pope A, Rivett AJ, Tavare JM. Rapid caspase-3 activation during apoptosis revealed using fluorescence-resonance energy transfer. EMBO Rep. 2000;1:266–270.

7 Rehm M, Dussmann H, Janicke RU, Tavare JM, Kogel D, Prehn JHM. Single-cell fluorescence resonance energy transfer analysis demonstrates that caspase activation during apoptosis is a rapid process: role of caspase-3. J Biol Chem. 2002;277:24506–24514.

8 Luo KQ, Yu VC, Pu Y, Chang DC. Measuring dynamics of caspase-8 activation in a single living HeLa cell during TNFα-induced apoptosis. Biochem Biophys Res Commun. 2003;304:217–222.

9 Takemoto K, Nagai T, Miyawaki A, Miura M. Spatio-temporal activation of caspase revealed by indicator that is insensitive to environmental effects. J Cell Biol. 2003;160:235–243.

10 Tsien RY. The green fluorescent protein. Annu Rev Biochem. 1998;67:509–544.

11 Kawai H, Suzuki T, Kobayashi T, Mizuguchi H, Hayakawa T, Kawanishi T. Simultaneous imaging of initiator/effector caspase activity and mitochondrial membrane potential during cell death in living HeLa cells. Biochim Biophys Acta. 2004;1693:101–110.

12 Zimmermann T, Rietdorf J, Pepperkok R. Spectral imaging and its applications in live cell microscopy. FEBS Lett. 2003;546:87–92.

13 Mizuno H, Sawano A, Eli P, Hama H, Miyawaki A. Red fluorescent protein from Discosoma as a fusion tag and a partner for fluorescence resonance energy transfer. Biochemistry. 2001;40:2502–2510.

14 Erickson MG, Moon DL, Yue DT. DsRed as a potential FRET partner with CFP and GFP. Biophys J. 2003;85:599–611.

15 Karasawa S, Araki T, Nagai T, Mizuno H, Miyawaki A. Cyan-emitting and orange-emitting fluorescent proteins as a donor /acceptor pair for fluorescence resonance energy transfer. Biochem J. 2004;381:307–312.

Available online at www.sciencedirect.com
SCIENCE DIRECT®
Journal of Chromatography A, 1067 (2005) 145–152
JOURNAL OF CHROMATOGRAPHY A
www.elsevier.com/locate/chroma

Isotope tag method for quantitative analysis of carbohydrates by liquid chromatography–mass spectrometry

Jin Yuan[1], Noritaka Hashii, Nana Kawasaki*, Satsuki Itoh, Toru Kawanishi, Takao Hayakawa

Division of Biological Chemistry and Biologicals, National Institute of Health Sciences, 1-18-1 Kamiyoga, Setagaya-ku, Tokyo 158-8501, Japan

Available online 15 December 2004

Abstract

We have previously demonstrated that liquid chromatography/mass spectrometry equipped with a graphitized carbon column (GCC-LC/MS) is useful for the structural analysis of carbohydrates in a glycoprotein. Here, we studied the monosaccharide composition analysis and quantitative oligosaccharide profiling by GCC-LC/MS. Monosaccharides were labeled with 2-aminopyridine and then separated and monitored by GCC-LC/MS in the selective ion mode. The use of tetradeuterium-labeled pyridylamino (d_4-PA) monosaccharides as internal standards, which were prepared by the tagging of standard monosaccharides with hexadeuterium-labeled 2-aminopyridine (d_6-AP), afforded a good linearity and reproducibility in ESIMS analysis. This method was successfully applied to the monosaccharide composition analysis of model glycoproteins, fetuin, and erythropoietin. For quantitative oligosaccharide profiling, oligosaccharides released from an analyte and a standard glycoprotein were tagged with d_0- and d_6-AP, respectively, and an equal amount of d_0- and d_4-PA oligosaccharides were coinjected into GCC-LC/MS. In this procedure, the oligosaccharides that existed in either analyte or a standard glycoprotein appeared as single ions, and the oligosaccharides that existed in both analyte and a standard glycoprotein were detected as paired ions. The relative amount of analyte oligosaccharides could be determined on the basis of the analyte/internal standard ion-pair intensity ratio. The quantitative oligosaccharide profiling enabled us to make a quantitative and qualitative comparison of glycosylation between the analyte and standard glycoproteins. The isotope tag method can be applicable for quality control and comparability assessment of glycoprotein products as well as the analysis of glycan alteration in some diseases.

Keywords: Monosaccharides; Oligosaccharides; Pyridylamination; Isotope tag

1. Introduction

A variety of recombinant glycoproteins and modified glycoproteins are developed as medical agents, and most of them exist in heterogeneous forms because of the various combinations of oligosaccharides. Alteration of glycosylation is known to affect the biological activity, mobilization, and biophysical properties of glycoproteins [1], so assessments of their carbohydrate structure and heterogeneity are essential in many stages of development and quality control of glycoprotein products. Since glycosylation varies in response to changes in the manufacturing condition, monosaccharide composition analysis and/or oligosaccharide profiling are needed for the characterization and as a test for constancy and comparability assessments of glycosylation [2]. Several analytical procedures using HPLC have been reported for oligosaccharide profiling and structural analysis of carbohydrates [3–5]. The oligosaccharide profiling using liquid chromatography/mass spectrometry (LC/MS) is especially known to provide structural information from their chromatographic behavior and molecular mass [6–8]. We have developed mass spectrometric oligosaccharide profiling using a graphitized carbon column (GCC), which can separate

Abbreviations: AP, 2-aminopyridine; d_0, non-deuterium-labeled; d_4, tetradeuterium-labeled; d_6, hexadeuterium-labeled; Fuc, fucose; Gal, galactose; GalN, galactosamine; GalNAc, *N*-acetylgalactosamine; GCC, graphitized carbon column; Glc, glucose; GlcN, glucosamine; GlcNAc, *N*-acetylglucosamine; Man, mannose; PA, pyridylamino; R.S.D., relative standard deviation; SIM, selected ion mode; TFA, trifluoroacetic acid; TIC, total ion chromatogram

* Corresponding author. Tel.: +81 3 3700 1141; fax: +81 3 3707 6950.
E-mail address: nana@nihs.go.jp (N. Kawasaki).
[1] Present address: Chendu Institute of Biological Products, 610063, Chengdu Wai Dong Bao Jiang Qiao, Sichuan Province, China.

0021-9673/$ – see front matter © 2004 Elsevier B.V. All rights reserved.
doi:10.1016/j.chroma.2004.11.070

oligosaccharides based on subtle differences in branch, position, and linkage with volatile solution [9,10]. This method enables us to distinguish the glycosylation among some glycoprotein products produced in different cells [11].

A use of internal standards is known to improve the precision and linearity in quantitative analyses. Isotopic analogs of the analytes are currently the preferred internal standards for quantification by mass spectrometry (MS) procedures. For instance, Gygi et al. [12] demonstrated the approach for the accurate quantification of the proteins within complex mixture using isotope-coded affinity tags (ICATs). The use of the isotope-labeled carbohydrates as internal standards can make it possible to quantify the carbohydrates by LC/MS. Reductive pyridylamination is frequently used for the tagging of carbohydrates in HPLC analysis [13,14]. This derivatization is known to afford higher sensitivity in MS analysis [15], and PA oligosaccharides were reported to be separated by GCC [16]. Here, we study quantitative analysis of carbohydrates using tetradeuterium-labeled pyridylamino (d_4-PA) carbohydrates as internal standards. First, we study the monosaccharide composition analysis by using d_4-PA monosaccharides as internal standards. Next, the isotope tag method is used for the quantitative oligosaccharide profiling using recombinant human chorionic gonadotropin (rhCG) and human chorionic gonadotropin (hCG) as an analyte and standard glycoproteins, respectively.

2. Materials and methods

2.1. Materials

All monosaccharide standards were purchased from Seikagaku-kogyo (Tokyo, Japan). The pyridylamination apparatus (PALSTATION), reagents for the pyridylamination reaction, and PA monosaccharide standards were available from TaKaRa Biomedicals (Otsu, Japan). The hexadeuterium-labeled 2-aminopyridine (d_6-AP) was purchased from Wako (Osaka, Japan). Human chorionic gonadotropin (hCG) and recombinant hCG (rhCG) were bought from Sigma (St. Louis, MO, USA). *N*-glycosidase F was purchased from Roche Diagnostics. All other chemicals and reagents were of analytical grade and were commercially available.

2.2. Pyridylamination of monosaccharides

For the pyridylamination of amino sugars, free amino groups of monosaccharides (GlcN, GalN, 1–1000 pmol) were acetylated by incubation in 50 μl of methanol/pyridine/distilled water (30/15/10, v/v/v) with 2 μl of acetic anhydride for 30 min at room temperature. The mixture was dried using a vacuum centrifuge evaporator without heating. Acetic acid (50 μl), methanol (60 μl), and 10 μl of coupling reagent prepared by mixing 100 mg of AP was added to monosaccharides (Fuc, Gal, Glc, Man, GlcNAc, GalNAc, 1–1000 pmol). The mixture was heated at 90 °C for 20 min by PALSTATION, and the excess reagents were removed by evaporation under a stream of nitrogen gas at 60 °C for 20 min. Then 10 μl of a reducing reagent, prepared just before use by mixing 6 mg of borane–dimethylamine complex and 100 μl of acetic acid, was added, and the mixture was heated at 90 °C for 35 min. The reaction mixture was dried three times under a stream of nitrogen gas at 50 °C for 10 min. The residue was dissolved in water for LC/MS analysis. For the preparation of isotope analogs, the tetradeuterium-labeled PA (d_4-PA) monosaccharide, d_0-AP was just replaced by d_6-AP (Fig. 1).

2.3. Monosaccharide composition analysis of a glycoprotein

A glycoprotein (25 pmol) was placed in a hydrolysis tube fitted with a Teflon-lined screw cap. Fifty microliters of 2 M HCl-2M trifluoroacetic acid (TFA) was added to the sample, which was then heated at 100 °C for 6 h. Simultaneously, a set of monosaccharide standards, 100 pmol of Gal, Man, Glc, Fuc, GlcN, and GalN, was treated identically as the analytes. The solution obtained was freeze-dried. The monosaccharides obtained from the analyte glycoproteins and standard monosaccharides were tagged with non-deuterium-labeled 2-aminopyridine (d_0-AP) and d_6-AP, respectively. Each tagged oligosaccharide mixture was dissolved into purified water, and a mixture of d_0- and d_4-PA monosaccharides was injected into the GCC-LC/MS.

2.4. Preparation of N-linked oligosaccharides

N-linked oligosaccharides were released from hCG as described previously [17]. Briefly, hCG and rhCG (100 μg)

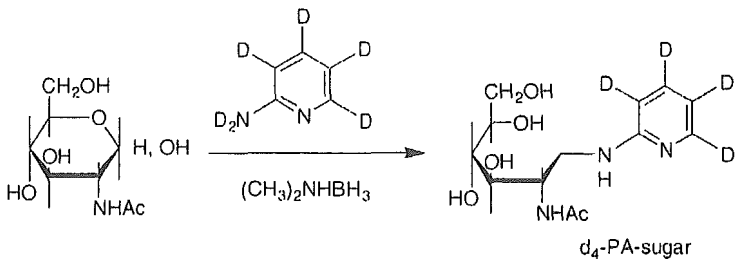

Fig. 1. Synthesis of d_4-PA monosaccharide internal standard.

were dissolved in 360 μl of 0.5 M Tris–HCl buffer (pH 8.6), containing 8 M guanidine hydrochloride and 5 mM ethylenediaminetetra-acetic acid (EDTA). After an addition of 2.6 μl of 2-mercaptethanol, the mixture was allowed to stand at room temperature for 2 h. To this solution, 7.56 mg of monoiodoacetic acid was added, and the resulting mixture was incubated at room temperature for 2 h in the dark. The reaction mixture was applied to a PD-10 column (Amershambioscience, Uppsala, Sweden) to remove the reagents, and the eluate was lyophilized.

Carboxymethylated hCG and rhCG were dissolved in 100 μl of 0.1 M sodium phosphate buffer, pH 7.2, and incubated with 5 units of PNGase F at 37 °C for 2 days. Protein was precipitated with 340 μl of cold ethanol, and the supernatant was dried.

2.5. Pyridylamination of oligosaccharides from hCG

To the lyophilized oligosaccharides released from rhCG we added 10 μl of coupling reagent prepared by mixing 300 mg of d_0-AP, and 100 μl of acetic acid, and the reaction mixture was heated at 90 °C for 60 min. Then, 10 μl of a reducing reagent, prepared just before use by mixing 20 mg of borane–dimethylamine complex and 100 μl of acetic acid, was added, and the mixture was heated at 80 °C for 60 min. The reaction mixture was dried three times under a stream of nitrogen gas at 60 °C for 10 min. The residue was dissolved in water for LC/MS analysis. For the preparation of the tetradeuterium-labeled (d_4)-PA oligosaccharide isotope analogs, d_0-AP was just replaced by d_6-2-aminopyridine.

2.6. LC/MS analysis

LC was carried out using a Magic 2002 HPLC system (Michrom BioResources Inc., Auburn, CA, USA) using a Hypercarb column (0.2 mm × 150 mm, Thermoelectron, San Jose, CA, USA). The flow rate was set at 2–3 μl/min through a splitter system. The mobile phases were 5 mM ammonium acetate (pH 8.5) with 2% of acetonitrile (pump A) and 80% of acetonitrile (pump B). A gradient of 10–35% of B in 60 min was used for the monosaccharide analysis. For oligosaccharide profiling, we used a gradient of 5–20% of B in 20 min, 20–70% of B in 15 min, and 70–95% of B in 5 min. The mass spectrometer used was a TSQ 7000 (Thermoelectron) equipped with a nanoelectrospray ion source (AMR Inc., Tokyo, Japan). The ESI voltage was set to 2000 V (positive ion mode) or 1500 V (negative ion mode), and the capillary temperature was 175 °C.

3. Results

3.1. Monosaccharide composition analysis using the isotope tag method

First, we examined the possibility of the isotope-tag method for the monosaccharide composition analysis of gly-

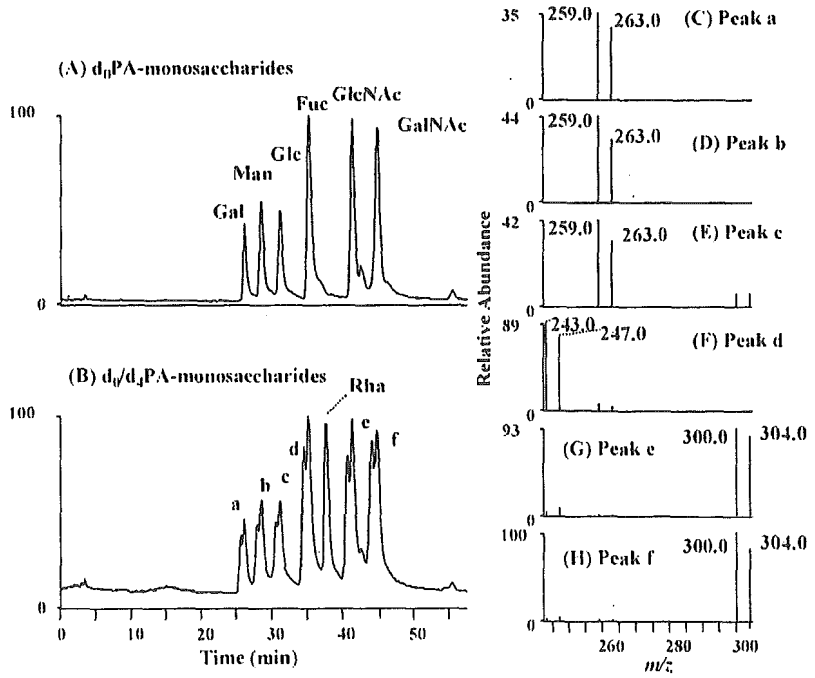

Fig. 2. (A) Extracted ion chromatogram (set *m/z* values, 243, 259, and 300) of d_0-PA monosaccharides (1 pmol Gal, Man, Glc, Fuc, GlcNAc, and GalNAc). (B) Extracted ion chromatogram (set *m/z* values, 243, 247, 259, 263, 300, and 304) of a mixture of d_0- and d_4-PA monosaccharides (1 pmol Gal, Man, Glc, Fuc, Rham, GlcNAc and GalNAc). (C) Mass spectra of peaks a (C), b (D), c (E), d (F), e (G), and f (H).

coproteins. An equal molar of each d_0-PA monosaccharide (Gal, Man, Glc, Fuc, GlcNAc, and GalNAc, 1 pmol each) was analyzed by GCC-LC/MS in the positive ion mode. The ions monitored were *m/z* 259 (for d_0-PA-Gal, d_0-PA-Man, and d_0-PA-Glc), *m/z* 243 (d_0-PA-Fuc), and *m/z* 300 (d_0-PA-GlcNAc and d_0-PA-GalNAc). Fig. 2A shows the mass chromatogram of the d_0-PA monosaccharides. All six d_0-PA monosaccharides were retained and separated by GCC. The detection limit at a signal-to-noise ratio of 3 was 45 fmol.

The d_4-PA monosaccharides were prepared as internal standards by tagging of standard monosaccharides with d_6-AP and combined with d_0-PA monosaccharides. Fig. 2B shows the chromatogram of a mixture of d_0-, d_4-PA monosaccharides and PA-labeled Rhamnose, which is frequently used as an internal standard in the monosaccharide composition analysis. Paired ions with a difference of *m/z* 4 were detected in the mass spectra of peaks a–f (Fig. 2C–H). When 0.5 pmol d_0-PA monosaccharides were determined in the presence of d_4-PA monosaccharides or Rhamnose by GCC-LC/MS, the relative standard deviation ($n = 5$) was 1.8–4.8% or 5.6–8.3%, respectively.

To assess the linearity and reproducibility of the whole procedure, including reacetylation, pyridylamination, the removal of excess derivatization reagents, and GCC-LC/MS, we tagged different amounts of monosaccharides (Gal, Man, Glc, Fuc, GlcN, and GalN, 1–1000 pmol) with d_0-AP, and d_4-PA monosaccharides (4 or 20 pmol) were added to the d_0-PA monosaccharides (1–10 pmol or 10–1000 pmol, respectively). The whole process of the isotope tag method was found to be linear for all six monosaccharides over the tested range of 1–1000 pmol (Fig. 3). The accuracy of this method was approximately 80–100% (Fig. 3), and the relative standard deviations (%R.S.D.) were less than 7.2% for all monosaccharides (based on the peak area ratio of monosaccharides from five samples).

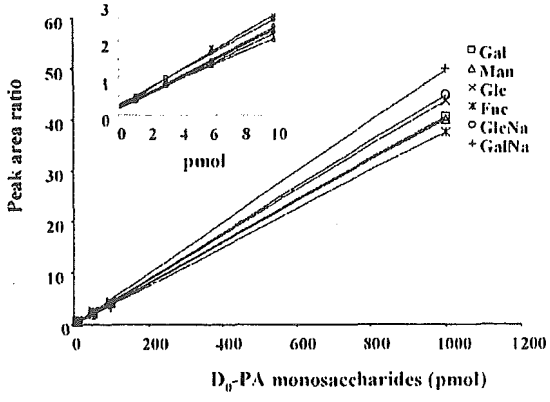

Fig. 3. Linearity on the isotope-tag method for monosaccharide quantification. For the internal standards, 1000 pmol monosaccharides were derivatized to d_4-PA monosaccharides. Different amounts of monosaccharides were derivatized to d_0-PA monosaccharides and co-injected with 4 pmol (A) or 20 pmol (B) internal standards into GCC-LC/MS.

We used this method for the monosaccharide composition analysis of fetuin and erythropoietin. Accuracy in the monosaccharide composition analysis of a glycoprotein relies on the condition of hydrolysis. Fan et al. [18] studied the hydrolysis of N-linked oligosaccharides and recommended 4 h with 2 M TFA at 100 °C for neutral sugars, and 6 h with 4 M HCl at 100 °C for amino sugars. While these hydrolysis conditions result in the complete release of neutral and amino sugars with no degradation, it takes two hydrolyses for a single sample. To quantify both neutral and amino sugars in glycoproteins in the same run, fetuin and erythropoietin (25 pmol) were heated in 2 M HCl-2M TFA at 100 °C for 6 h [19], and a set of monosaccharide standards, 100 pmol of Gal, Man, Glc, Fuc, GlcN, and GalN, was treated identically as the analyte glycoproteins. After hydrolysis, the analyte and standard monosaccharides were tagged with d_0- and d_6-AP, respectively. Fig. 4A and E show the mass chromatogram of monosaccharides prepared from fetuin and erythropoietin in the presence of d_4-PA monosaccharides, respectively.

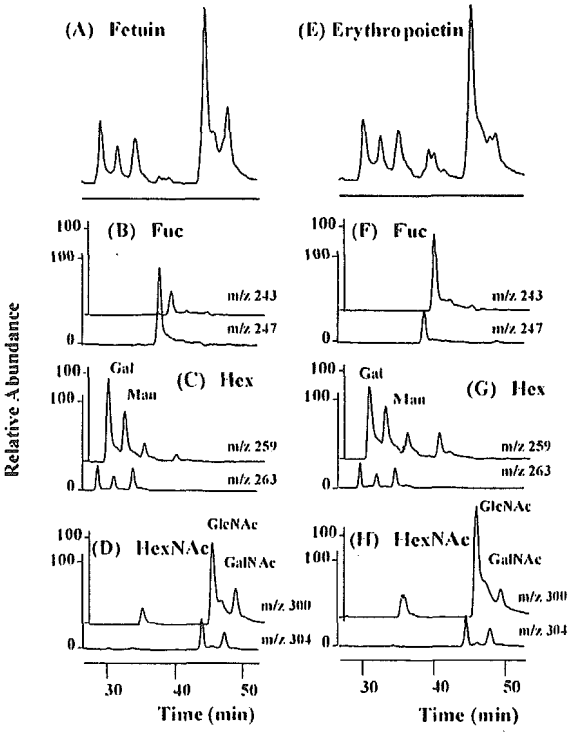

Fig. 4. Monosaccharide composition analysis of glycoproteins. Extracted ion chromatograms of d_0-PA monosaccharides from fetuin and d_4-PA standard monosaccharides (set *m/z* values, 243, 247, 259, 263, 300, and 304) (A), d_0-PA Fuc from fetuin and d_4-PA standard Fuc (set *m/z* values, 243 and 247) (B), d_0-PA Hex from fetuin and d_4-PA standard Hex (set *m/z* values, 259 and 263) (C), and d_0-PA HexNAc from fetuin and d_4-PA standard HexNAc and (set *m/z* values, 300 and 304) (D). Extracted ion chromatograms of d_0-PA monosaccharides from erythropoietin and d_4-PA standard monosaccharides and (set *m/z* values, 243, 247, 259, 263, 300, and 304) (E), d_0-PA Fuc from erythropoietin and d_4-PA standard Fuc (set *m/z* values, 243 and 247) (F), d_0-PA Hex from erythropoietin and d_4-PA standard Hex (set *m/z* values, 259 and 263) (G), and d_0-PA HexNAc from erythropoietin and d_4-PA standard HexNAc (set *m/z* values, 300 and 304) (H).

Table 1
Monosaccharide composition analysis by isotope-tag method

Glycoprotein	Monosaccharide	mol/mol[a]	mol/mol
Fetuin	Fuc	0.3	0 [20]
	Gal	10.4	12
	Man	7.6	9
	GlcNAc	14.7	15
	GalNAc	3.4	3
Erythropoietin	Fuc	3.4	4.1 [21]
	Gal	12.8	13.8
	Man	8.1	8.7
	GlcNAc	15.6	17.2
	GalNAc	1.5	0.9

[a] Values were expressed as mol detected in 1 mol glycoprotein.

Fig. 4B, and F show the mass chromatograms of d_0-, and d_4-PA fucose, Fig. 4C and G indicate those of d_0-, d_4-PA hexose, and Fig. 4D and H show those of d_0-, d_4-PA HexNAc. The monosaccharide compositions of fetuin and erythropoietin calculated from the peak area ratios (d_0-PA/d_4-PA monosaccharides) were in good agreement with the reported values (Table 1) [20,21]. By heating the standard monosaccharides simultaneously the decomposition of monosacchrides during hydrolysis can be corrected, and a use of isotope analogs as the internal standards can reduce deviation in ESIMS analysis.

3.2. *Quantitative oligosaccharide profiling using the isotope tag method*

Next, we explored the capability of the isotope-tag method for the quantitative oligosaccharide profiling. When d_0-PA oligosaccharides prepared from an analyte glycoprotein are analyzed with an equal part of d_4-PA oligosaccharides prepared from a standard glycoprotein, oligosaccharides which link to both the analyte and the standard glycoproteins are expected to appear as paired ions with a difference of 4 Da, and the individual oligosaccharides in the analyte glycoprotein can be quantified based on the analyte/internal standard ion-pair intensity ratio. On the other hand, any oligosaccharides that link to either the analyte or the standard glycoprotein ought to be detected as single ions. Oligosaccharides released from rhCG and hCG were tagged with d_0- and d_6-AP, respectively, and the tagged oligosaccharides were analyzed by GCC-LC/MS in both positive and negative ion modes.

Fig. 5A and B show the mass spectra of the peak which was detected at 21.5 min in the positive and the negative ion mode, respectively. In the positive ion mode, ions at *m/z* 863.0, 1359.4 and 1197.2 were detected (Fig. 5A), and they can be assigned to d_4-PA $[Hex]_5[HexNAc]_4^{2+}$ (an asialobiantennary oligosaccharide), d_4-PA$[Hex]_3[HexNAc]_4^+$ (a fragment of the asialobiantennary form) and d_4-PA$[Hex]_4[HexNAc]_4^+$ (a fragment of the asialobiantennary form), respectively. In contrast, only an ion at *m/z* 860.9 (d_4-PA$[Hex]_5[HexNAc]_4^{2-}$, asialobiantennary oligosaccharide) was detected in the negative ion mode (Fig. 5B). This result suggests that mass spectra

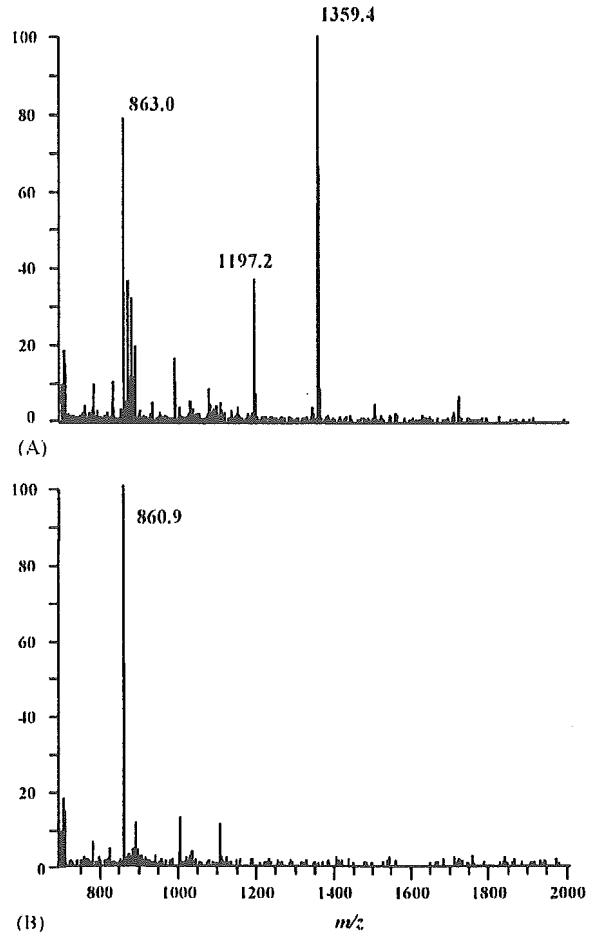

Fig. 5. Mass spectra of d_4-PA oligosaccharide. D_4-PA oligosaccharide eluted at 21.5 min from GCC was analyzed by ESIMS in the positive ion mode (A) and negative ion mode (B).

of PA oligosaccharides become complicated due to fragmentation in the positive ion mode, while only molecular ions can be detected in the negative ion mode. Therefore, ESI analysis in the negative ion mode was chosen for the PA oligosaccharide profiling.

Fig. 6A and B show the TIC of a mixture of equal parts of d_0-PA oligosaccharides prepared from rhCG and d_4-PA oligosaccharides from hCG, and its two-dimensional display (retention time versus *m/z*), respectively. The carbohydrate structures, which can be deduced from *m/z* values, are indicated in Table 2. Paired ions at *m/z* 757.5, 759.5 were observed in the mass spectrum of peak a1. Based on carbohydrate composition $[Hex]_5[HexNAc]_3$, it can be assigned to a hybrid type oligosaccharide. Likewise, peak 11, 12, 14, 15, p1, p2, and p4 consisted of paired ions and can be assigned to monosialylated (11, 12, 14, 15) and disialylated (p1, p2) biantennary oligosaccharide without Fuc. Fig. 7 shows TIC of d_0-, d_4-PA oligosaccharides (A), extracted ion chromatograms of d_0-PA (B), d_4-PA (C), and d_0-, d_4-PA monosialylated biantennary form (D). The mass spectra of peaks 11–15 are shown in Fig. 7E–I. Peak 13 was not observed in Fig. 7D and only

Table 2
Structural assignment of peaks in Fig. 6B

Peak nos.	Carbohydrate composition[a]	Deduced structure[b]	Theoretical mass (d_0-PA-sugar)	Observed *m/z*			Ion-pair intensity ratio d_0/d_4
				d_0-PA-rhCG	d_4-PA-hCG		
				M^{2-}	M^{3-}	M^{2-}	
a1	$[Hex]_5[HexNAc]_3$	Hybrid (1)	1517.5	757.5		759.5	0.27
b1	$[Hex]_5[HexNAc]_4[NeuNAc]_2$	Bi + NA_2	2303.1		768.2		
c1	$[Fuc]_1[Hex]_5[HexNAc]_4[NeuNAc]_2$	FBi + NA_2	2449.3		816.7		
d1	$[Hex]_4[HexNAc]_3[NeuNAc]_1$	Mono + NA	1646.6			824.3	
d2	$[Hex]_4[HexNAc]_3[NeuNAc]_1$	Mono + NA	1646.6			824.0	
e1	$[Hex]_6[HexNAc]_3$	Hybrid (2)	1679.6	838.6			
e2	$[Hex]_6[HexNAc]_3$	Hybrid (2)	1679.6			840.6	
f1	$[Hex]_5[HexNAc]_4$	Bi	1720.7	858.9			
f2	$[Hex]_5[HexNAc]_4$	Bi	1720.7			861.2	
g1	$[Hex]_5[HexNAc]_3[NeuNAc]_1$	Hybrid (1) + NA	1807.7	902.9			
g2	$[Hex]_5[HexNAc]_3[NeuNAc]_1$	Hybrid (1) + NA	1808.7			905.0	
h1	$[Fuc]_1[Hex]_5[HexNAc]_4$	FBi	1866.8			934.0	
i1	$[Hex]_6[HexNAc]_4$	Hybrid (3)	1882.8	940.2			
j1	$[Hex]_5[HexNAc]_5$	Bi + GN	1924.9			962.7	
k1	$[Hex]_6[HexNAc]_3[NeuNAc]_1$	Hybrid (2) + NA	1970.8			986.8	
k2	$[Hex]_6[HexNAc]_3[NeuNAc]_1$	Hybrid (2) + NA	1970.8			986.2	
l1	$[Hex]_5[HexNAc]_4[NeuNAc]_1$	Bi + NA	2011.9	1004.7		1006.7	0.77
l2	$[Hex]_5[HexNAc]_4[NeuNAc]_1$	Bi + NA	2011.9	1004.6		1007.3	0.56
l3	$[Hex]_5[HexNAc]_4[NeuNAc]_1$	Bi + NA	2011.9	1004.6			
l4	$[Hex]_5[HexNAc]_4[NeuNAc]_1$	Bi + NA	2011.9	1004.6		1006.5	0.67
l5	$[Hex]_5[HexNAc]_4[NeuNAc]_1$	Bi + NA	2011.9	1004.6		1006.4	0.49
m1	$[Hex]_7[HexNAc]_4$	Hybrid (4)	2044.9	1021.4			
n1	$[Fuc]_1[Hex]_5[HexNAc]_4[NeuNAc]_1$	FBi + NA	2158.0			1079.8	
n2	$[Fuc]_1[Hex]_5[HexNAc]_4[NeuNAc]_1$	FBi + NA	2158.0			1079.8	
n3	$[Fuc]_1[Hex]_5[HexNAc]_4[NeuNAc]_1$	FBi + NA	2158.0			1079.8	
o1	$[Hex]_6[HexNAc]_4[NeuNAc]_1$	Hybrid (3) + NA	2174.0	1085.6			
o2	$[Hex]_6[HexNAc]_4[NeuNAc]_1$	Hybrid (3) + NA	2174.0	1085.7			
p1	$[Hex]_5[HexNAc]_4[NeuNAc]_2$	Bi + NA_2	2303.1	1150.3		1152.1	5.76
p2	$[Hex]_5[HexNAc]_4[NeuNAc]_2$	Bi + NA_2	2303.1	1150.2		1152.2	5.92
p3	$[Hex]_5[HexNAc]_4[NeuNAc]_2$	Bi + NA_2	2303.1	1150.1			
p4	$[Hex]_5[HexNAc]_4[NeuNAc]_2$	Bi + NA_2	2303.1	1150.3		1152.4	0.45

[a] Hex, hexsose; HexNAc, *N*-acetyl hexsosamine; NeuNAc, *N*-acetyl neuraminic acid; Fuc, fucose.
[b] Abbreviations and structures. The structures are based on the previous reports.

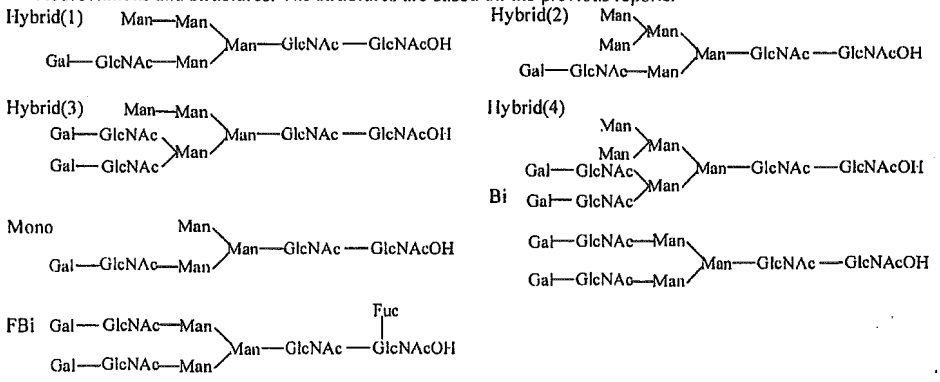

single ion was detected in Fig. 7G. These results suggest that one of monosialylated binantenary oligosaccharides isomers links to only rhCG.

We determined relative amounts of some oligosaccharides in rhCG on the basis of ion-pair intensity ratios (Table 2). The amount of monosialylated biantennary forms (l1, l2, l4, and l5) linked to rhCG were 50–70% of those to hCG. The amount of disialylated biantennary forms (p1 and p2) linked to rhCG was five-fold of those to hCG, and the linkage of p4 to rhCG was one-half of that of hCG. The isotope tag method clearly shows the difference in distribution of isomers between rhCG and hCG.

In this procedure, oligosaccharides linked to either rhCG or hCG were detected as single ions. As shown in Table 2, nine oligosaccharides were detected as single ions in rhCG, and they are reduced to hybrid type and complex type.